

## Experimental and theoretical cross sections for $K$ -shell ionization of $_{52}\text{Te}$ , $_{73}\text{Ta}$ , and $_{83}\text{Bi}$ by electrons with energies up to 100 keV

O. C. B. Santos, V. R. Vanin,\* N. L. Maidana, M. N. Martins, M. H. Tabacniks, C. L. Rodrigues, T. F. Silva, and A. D. Santos  
*Instituto de Física, Universidade de São Paulo, Rua do Matão 1371, Cidade Universitária, CEP 05508-090, São Paulo, Brazil*

S. F. Barros

*Instituto Federal de São Paulo, Rua Primeiro de Maio 500, Estação Itaquaquecetuba, CEP 08571-050, São Paulo, Brazil*

J. A. García-Alvarez

*Physical Sciences Department, College of Southern Nevada, 6375 West Charleston Boulevard, Las Vegas, Nevada 89146, USA*

M. F. Koskinas

*Instituto de Pesquisas Energéticas e Nucleares, CNEN/SP, Avenida Lineu Prestes 2242, Cidade Universitária, CEP 05508-000, São Paulo, Brazil*

J. M. Fernández-Varea 

*Departament de Física Quàntica i Astrofísica and Institut de Ciències del Cosmos, Facultat de Física, Universitat de Barcelona, Diagonal 645, 08028 Barcelona, Catalonia, Spain*

M. S. Pindzola

*Department of Physics, Auburn University, Auburn, Alabama 36849, USA*



(Received 7 May 2019; published 7 August 2019)

In this work we present a combined experimental and theoretical study of  $K$ -shell ionization by electrons with energies close to the threshold. The ionization cross sections of the  $K$  shells of Te, Ta, and Bi atoms have been measured up to 100 keV with uncertainties ranging from 4% to 8%. In turn, calculations have been done using the subconfiguration average distorted-wave (SCADW) method, which includes the full two-body retarded electromagnetic interaction between the projectile and target electrons. The predictions of the SCADW method are in good agreement with the experimental data. In contrast, theoretical cross sections based on first-order perturbation theory where the transverse interaction is computed with plane waves instead of distorted waves underestimate the SCADW values as well as the experimental data. The difference between the two investigated *ab initio* formalisms grows with atomic number, being 3% for Te, 15% for Ta, and 25% for Bi. An additional comparison of both theoretical approaches with recent measurements for Au  $K$  supports the conclusion that the SCADW method reproduces well the experimental  $K$ -shell ionization cross section of atoms with intermediate to large  $Z$  near the threshold.

DOI: [10.1103/PhysRevA.100.022703](https://doi.org/10.1103/PhysRevA.100.022703)

### I. INTRODUCTION

The ionization of atomic inner shells by electron impact is a fundamental collision process whose dynamics can be studied using x rays as a tracer. The corresponding cross sections are still known with uncertainties around 10% or larger despite the long history of this subject, more than 120 years after Röntgen's discovery of x rays.

Llovet *et al.* [1] compiled and reviewed critically the existing experimental cross sections for the ionization of  $K$ ,  $L$ , and  $M$  (sub)shells by electron impact. Measurements at electron energies close to the threshold are scarce for the  $K$  shells of atoms with intermediate or large  $Z$ . In particular, for  $Z \geq 43$  and  $E \leq 100$  keV a reasonable number of data were

reported just for  $_{47}\text{Ag}$  and  $_{79}\text{Au}$ , and a few isolated values exist for  $_{50}\text{Sn}$ ,  $_{51}\text{Sb}$ ,  $_{56}\text{Ba}$ ,  $_{57}\text{La}$ , and  $_{59}\text{Pr}$ . Only a small subset of these cross sections was identified as superior data by Llovet and co-workers, and often the measurements are discrepant.

Bote and Salvat [2] employed the relativistic first Born approximation to carry out systematic calculations of inner-shell ionization cross sections. Their formalism starts from the Coulomb gauge wherein the electron-atom interaction is expressed as the sum of longitudinal and transverse contributions. The longitudinal term is evaluated using distorted waves for the initial and final wave functions of the projectile and target electrons. However, to simplify the mathematical expression of the transverse term, the projectile electron is described with plane waves. This calculation scheme, referred to as the distorted-wave Born approximation (DWBA), was thoroughly assessed in the aforementioned review [1]. It was found that the predictions of the DWBA were in satisfactory

\*vanin@if.usp.br

agreement with the body of experimental cross sections. The database of DWBA ionization cross sections is endorsed by the National Institute of Standards and Technology (NIST) [3] and it has been implemented in Monte Carlo codes for coupled electron-photon transport [4].

Following the review by Llovet *et al.*, Fernández-Varea *et al.* [5] presented experimental ionization cross sections for the  $K$  shells of Au and Bi near the threshold and noticed that the DWBA underestimates the measurements by  $\sim 20\%$ . However, the uncertainties of their experimental results are around 11% or greater because they were obtained from relative measurements normalized to bremsstrahlung cross sections whose uncertainties are  $\sim 10\%$ . New experimental data with smaller uncertainties are thus needed to ascertain whether the observed behavior of the DWBA cross sections is systematic and to better quantify the discrepancy.

The transverse interaction is of the order of  $(v/c)^2$  and therefore its effect is appreciable only for projectiles with relativistic velocities. Since the binding energy of  $K$ -shell electrons in high- $Z$  atoms is several tens of keV, the transverse term is expected to be important even close to the threshold. Hence, the use of plane waves instead of distorted waves to evaluate this term may introduce sizable errors in the calculated ionization cross sections.

Ionization cross sections can also be calculated having recourse to the subconfiguration average distorted-wave (SCADW) formalism, based on first-order perturbation theory (Lorentz gauge), which adopts distorted waves for all continuum electron states. The SCADW method was developed by Pindzola *et al.* [6,7] and was used extensively to compute cross sections for electron-ion impact ionization in plasmas of interest to astrophysics and fusion research. More recently, this method has been applied to the ionization of neutral atoms. In a very recent publication, Pindzola [8] showed that the predictions of the SCADW formalism are in good agreement with the experimental Au  $K$  cross sections reported in [5] when the full two-body retarded electromagnetic interaction is included in the calculations. Nevertheless, he underscored the need for more measurements on high- $Z$  elements.

In this context, the purpose of the present work is to provide experimental and theoretical  $K$ -shell ionization cross sections for a few atoms with intermediate to large  $Z$ . The experimental design and setup used in [5] was improved [9,10] and employed to measure the cross sections for the  $K$  shells of  $^{52}\text{Te}$ ,  $^{73}\text{Ta}$ , and  $^{83}\text{Bi}$  with small uncertainties. Furthermore, calculations were done for these elements using the SCADW method with the full two-body retarded electromagnetic interaction so as to investigate the performance of this formalism.

The rest of the article is structured as follows. The experimental method and subsequent data analysis procedure are explained in Secs. II and III, respectively. The SCADW methodology is outlined in Sec. IV. Section V presents the measured and calculated ionization cross sections and discusses the results. Our conclusions are summarized in Sec. VI.

## II. EXPERIMENTAL METHOD

The cross sections were determined from the characteristic x-ray yields measured with two high-purity germanium

(HPGe) detectors, using electron beams with energies from the  $K$ -shell ionization threshold to 100 keV. The areal densities of atoms (number of atoms per unit surface) and the beam current were measured directly, the former by Rutherford backscattering spectrometry (RBS) and the latter summing the charges collected in the Faraday cup and the irradiation chamber. Although a detailed description of the beamline and the experimental arrangement can be found in [10] and references cited therein, we provide below a concise explanation of the experimental procedures linked to the improvement in the precision of the results.

### A. Target preparation

The target frames were made of 0.3-mm-thick C fiber with a 10-mm circular opening in the center of a 30 mm  $\times$  15 mm rectangle. The holes in the frames were covered with C film whose mass thickness is 10–15  $\mu\text{g}/\text{cm}^2$ . Films of  $\text{TeO}_2$ , Ta, and  $\text{Bi}_2\text{O}_3$  were deposited on these backings, the oxides by vapor deposition and Ta by sputtering from a metallic disk, through a mask that limited the target surface area to a circle 8 mm in diameter, in both deposition techniques. The use of thin C frames reduces bremsstrahlung by the electron-beam halo, and restricting the target material to a small area minimizes ionization by stray photons and electrons.

### B. Areal densities

The manufactured Te/C, Ta/C, and Bi/C targets were characterized by RBS. Measurements using 2200(11)-keV  $^4\text{He}^+$  ions were performed at the Laboratory of Materials Analysis with Ion Beams of the University of São Paulo. The experimental setup consisted of a Si surface barrier detector to measure the energy spectra of ions backscattered at  $120.0(5)^\circ$  with respect to the beam direction. The beam current was kept at approximately 10 nA and all spectra were recorded until an integrated charge of 10.0  $\mu\text{C}$  was reached. A cylindrical shielding at a negative potential mitigated the losses due to the emission of secondary electrons, providing good accuracy in the measurements of deposited charge. The beam spot, defined by a Ta collimator, was 1.8 mm in diameter and the incidence angle with respect to the target surfaces was  $7^\circ$  opposite to the detector direction.

The evaluation of the RBS spectra was carried out using the MULTISIMNRA [11] software, which relies on the physical modeling and simulations furnished by the SIMNRA code [12]. MULTISIMNRA follows a reverse Monte Carlo method [13], varying the sample profile to optimize an objective function that compares the experimental spectra with the simulations. The result of the sample characterization emerges from the optimization algorithm as the adjustable parameters that yield a simulated spectrum displaying the best consistency with the experimental data. The main advantage of MULTISIMNRA is the feature that explores the solution space to check how sensitive the result is to variations of the fitting parameters. This procedure furnishes a robust assessment of the influence of the main uncertainty sources on the result including correlations. Typical RBS spectra of the three samples are presented in Fig. 1 together with the simulated spectra for the profiles fitted by MULTISIMNRA.

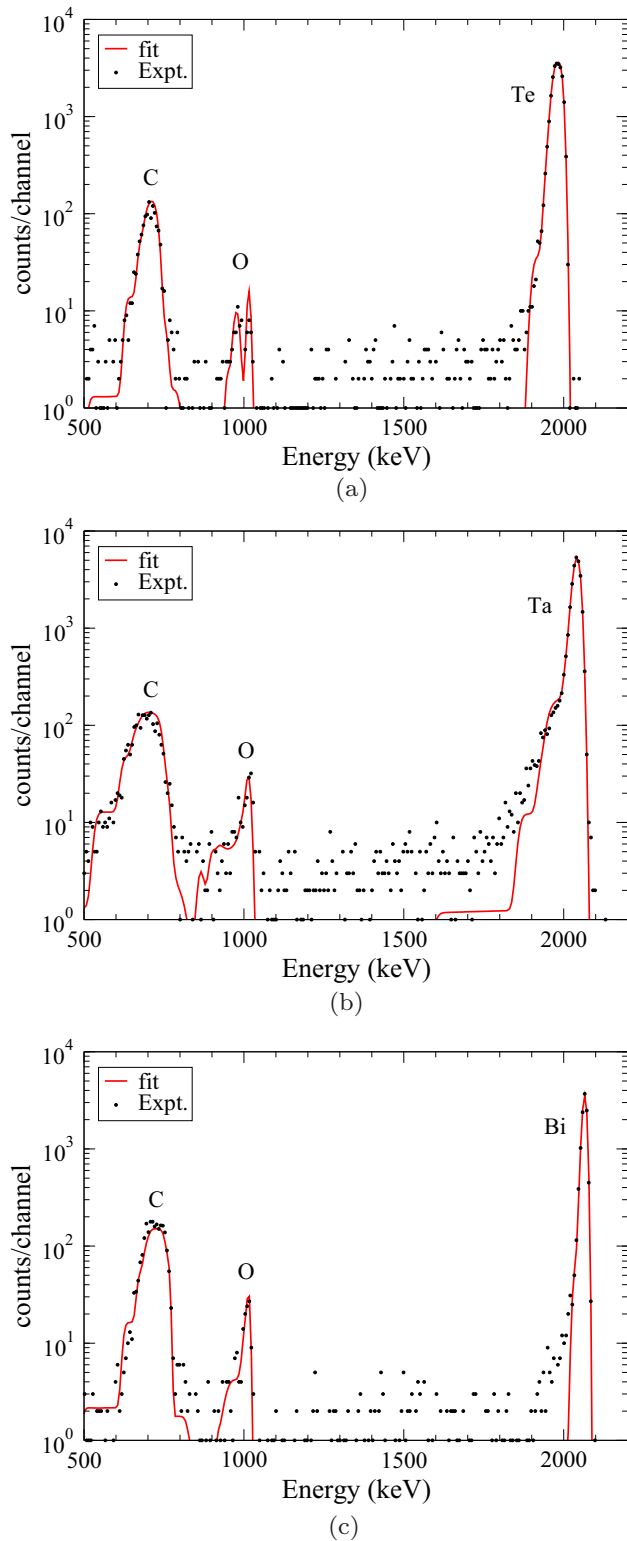


FIG. 1. RBS spectra of 2200-keV  ${}^4\text{He}^+$  ions incident on the (a) Te/C, (b) Ta/C, and (c) Bi/C targets. The dots are the experimental values and the curves are the MULTISIMNRA simulated spectra. The energy dispersion is approximately 6 keV/channel in all cases.

As input for fundamental physics parameters, all simulations were done with the SRIM2010 [14] stopping powers and the screening function of Andersen *et al.* to correct the Rutherford elastic differential cross section [15]. The

TABLE I. The first three columns indicate the various sources of uncertainty, the corresponding types, and their relative standard deviations (in %). The last three columns give the relative standard deviations of the areal density of Te, Ta, and Bi atoms in the RBS measurement (in %) due to the uncertainty source listed in the first column.

Parameter	Type <sup>a</sup>	Rel. unc. <sup>b</sup>	Te <sup>c</sup>	Ta <sup>c</sup>	Bi <sup>c</sup>
beam energy	A	0.5	0.9	0.6	1.0
electronics gain	B	0.3	2.9	3.1	3.1
electronics offset	B	0.3			
charge integration	A	0.5	1.8	0.5	0.8
scattering angle	B	0.4	1.1	1.2	0.7
stopping power	B	1.0	1.0	0.6	1.3
total uncertainty			3.8	3.5	3.6

<sup>a</sup>According to the definitions in [17].

<sup>b</sup>Relative uncertainty. Offset uncertainty is relative to the energy of the peak of interest.

<sup>c</sup>Relative propagated uncertainty.

empirical formula of Yang *et al.* [16] was selected to describe energy-loss straggling. Despite variations in the stopping power model, all other fundamental parameters were assumed to have negligible uncertainty.

Table I summarizes the main uncertainty sources in the RBS measurements for each target and its propagation to the quantitative value of the areal density of atoms. The propagation includes calculations using MULTISIMNRA to explore the solution space within the limits defined by the uncertainties.

The areal densities  $\mathcal{N}d$  ( $\mathcal{N}$  is the number of atoms per unit volume and  $d$  is the film thickness) of Te, Ta, and Bi atoms and their uncertainties (one standard deviation) are, respectively, 102(4), 59.5(21), and 17.8(6) in units of  $10^{15}$  atoms/cm<sup>2</sup>. These values correspond to mass thicknesses equal to 21.6(8), 17.9(6), and 6.2(2)  $\mu\text{g}/\text{cm}^2$ .

### C. Beamline

The 100-keV beamline of the São Paulo Microtron, which delivers electrons with kinetic energies between 10 and 100 keV from its gun, was employed. The current varied between 10 and 100 nA. The beam spot on target was around 2 mm in diameter. The energy dispersion was  $\lesssim 100$  eV (one standard deviation) in all irradiation runs.

The cylindrical irradiation chamber (inner diameter 490 mm, height 300 mm) is made of stainless steel with Al lids and it is kept electrically insulated from the ground. The base pressure was  $1.3 \times 10^{-4}$  Pa during the experiment. The targets were placed in the center of the chamber, perpendicularly to the electron beam (incidence angle  $\alpha = 0^\circ$ ). The Faraday cup is made of graphite, shaped as a truncated cone with a  $12^\circ$  half-aperture and with its bottom located at about twice the radius of the irradiation chamber so as to keep this unwanted photon source small and far from the target [10]. The charges collected by the Faraday cup and the chamber were integrated and summed to yield the number of incident electrons  $N_e$  with an accuracy better than 0.5%.

#### D. X-ray detection

Two planar HPGe spectrometers with thin Be windows, purchased from ORTEC, were used. One of them was a GLP series with a volume of 8 cm<sup>3</sup> (nominal crystal thickness 10 mm and radius 16 mm), positioned at an angle  $\theta_1 = 35^\circ$  with respect to the electron beam. The other was a 1000 series with a volume of 5 cm<sup>3</sup> (nominal crystal thickness 10 mm and radius 12.5 mm), mounted at  $\theta_2 = 131^\circ$  with respect to the beam. Their FWHM energy resolutions were 650 eV at 122 keV. Collimators 70 mm in length and 10 mm in diameter made of Cu were placed in front of the detectors and the whole arrangement was shielded with Pb bricks.

The two spectrometers were calibrated in energy for each run, fitting the parameters of a first-degree polynomial, choosing as standards the energies of  $K$  and  $L$  x rays in the cases of Ta and Bi, and  $K\alpha$  and  $K\beta$  for Te, taken from [18]. Figure 2 displays the  $K\alpha$  x-ray region of a few representative energy spectra generated by the Te/C, Ta/C, and Bi/C targets, recorded with both detectors, featuring the striking difference in the ratios between characteristic x-ray and bremsstrahlung intensities at the two detection angles.

The full-energy peak efficiency  $\varepsilon_{\text{FE}}$  of the spectrometers was measured using <sup>57</sup>Co, <sup>133</sup>Ba, <sup>152</sup>Eu, and <sup>241</sup>Am radioactive sources that were prepared and had their activities calibrated at the Nuclear Metrology Laboratory, Research Institute and National Commission for Nuclear Energy, São Paulo. Specifically, each source was manufactured as follows. First, a C fiber frame identical to those described above was covered with an approximately 7.5- $\mu\text{m}$ -thick Kapton foil and a very thin collodion film. Next, one drop of acid solution containing the radionuclide, carrier-free, was deposited in the center. After drying up, the radioactive material was covered with another collodion film and the complete source was sealed with a second Kapton foil.

The sources were placed in the target position, with the irradiation chamber filled with air, and the experimental  $\varepsilon_{\text{FE}}$  values were deduced from the net areas of the various  $\gamma$ -ray peaks observed in the acquired spectra. The parameters of Seltzer's analytical efficiency model [19], namely, the fraction of solid angle  $\Omega/(4\pi \text{ sr})$  and the thickness  $L$  of the Ge crystal, were fitted to the experimental data; the ensuing values were  $\Omega_1/(4\pi \text{ sr}) = 3.94(3) \times 10^{-5}$  and  $L_1 = 8.35(18) \text{ mm}$  for the detector at  $\theta_1$ , and  $\Omega_2/(4\pi \text{ sr}) = 3.15(2) \times 10^{-5}$  and  $L_2 = 10.3(2) \text{ mm}$  for the detector at  $\theta_2$ . Seltzer's model without the attenuation factors associated with the air in the irradiation chamber and with the Kapton covers of the calibration sources was used to evaluate the full-energy peak efficiencies at any photon energy  $E$ . Figure 3 depicts the experimental values along with the  $\varepsilon_{\text{FE}}(E)$  curves calculated with the fitted parameters for both detectors.

#### E. Electron-beam energy

The electron-beam energy in each run was determined from the tip of the bremsstrahlung spectra as described in [9]. In brief, a Gaussian energy profile is convolved with the bremsstrahlung spectrum calculated according to [20,21] and with the Gaussian profile of the peaks observed for monoenergetic photons in the x-ray spectrometers. The electron-beam energy spread and average parameters are simultaneously

fitted to the experimental photon energy spectrum. We quote in Sec. V the mean of the beam energy average parameters fitted to the spectra acquired with the two HPGe detectors.

### III. DATA ANALYSIS

The experimental  $K\alpha$  x-ray production cross sections were deduced from the expression

$$\sigma_{K\alpha}^x(E) = N_{K\alpha} \left[ N_e \frac{\mathcal{N}d}{\cos \alpha} \varepsilon_{\text{FE}}(E_{K\alpha}) \tau \right]^{-1}, \quad (1)$$

with all quantities on the right-hand side determined experimentally. The peak areas  $N_{K\alpha}$  of the prominent  $K\alpha_{1,2}$  doublet were extracted from least-squares fits of the parameters of two Voigt functions and a linear background to the observed peaks using the procedure described in [22]. The peak positions were left free to vary except in the case of Te, where a fixed energy difference  $E_{K\alpha_1} - E_{K\alpha_2}$ , taken from [18], was enforced because the Te  $K\alpha_{1,2}$  lines overlap strongly [see Figs. 2(a) and 2(b)]. The number of incident electrons in each run  $N_e$  and the areal density of atoms in the three targets  $\mathcal{N}d$  were measured as described in the preceding section. Recall that the incidence angle  $\alpha$  was set to  $0^\circ$ . Considering that the full-energy peak efficiencies for  $K\alpha_1$  and  $K\alpha_2$  x rays differ by only a fraction of a percent, we evaluated  $\varepsilon_{\text{FE}}$  at the energy  $E_{K\alpha}$ , which is the average of the  $K\alpha_1$  and  $K\alpha_2$  transition energies weighted with their intensities (emission rates) [23]. The last factor  $\tau = t_{\text{live}}/t_{\text{beam}}$  corrects for the difference (a few percent) between the x-ray detector live time  $t_{\text{live}}$  and the irradiation elapsed time  $t_{\text{beam}}$ .

The  $K$ -shell ionization cross sections were then determined by means of the relation

$$\sigma_K(E) = \sigma_{K\alpha}^x(E) \left[ \omega_K \frac{\Gamma_{KL_{2,3}}}{\Gamma_{K,\text{total}}} \right]^{-1}, \quad (2)$$

where  $\omega_K$  is the  $K$ -shell fluorescence yield and  $\Gamma_{KL_{2,3}}/\Gamma_{K,\text{total}}$  is the ratio of x-ray emission rates. We adopted Krause's semiempirical fluorescence yields [24] and Scofield's Dirac-Hartree-Slater emission rates [23].

### IV. SCADW CALCULATIONS

The theoretical evaluation of the  $K$ -shell electron-impact ionization cross section for an intermediate- to high- $Z$  atom demands a considerable computational effort because it requires one to take into account the distortions of the projectile and active electron wave functions caused by the screened potential of the target atom as well as exchange and relativistic effects.

For direct ionization a general transition between relativistic subconfigurations has the form

$$(n_0 \ell_0 j_0)^{w_0} p_i \ell_i j_i \rightarrow (n_0 \ell_0 j_0)^{w_0-1} p_e \ell_e j_e p_f \ell_f j_f, \quad (3)$$

where  $n_0 \ell_0 j_0$  are quantum numbers of the bound electron and  $w_0$  is the corresponding (sub)shell occupation number, whereas  $p_i \ell_i j_i$ ,  $p_e \ell_e j_e$ , and  $p_f \ell_f j_f$  are quantum numbers of the initial, ejected, and final continuum electrons, respectively. The SCADW ionization cross section (in atomic units) is

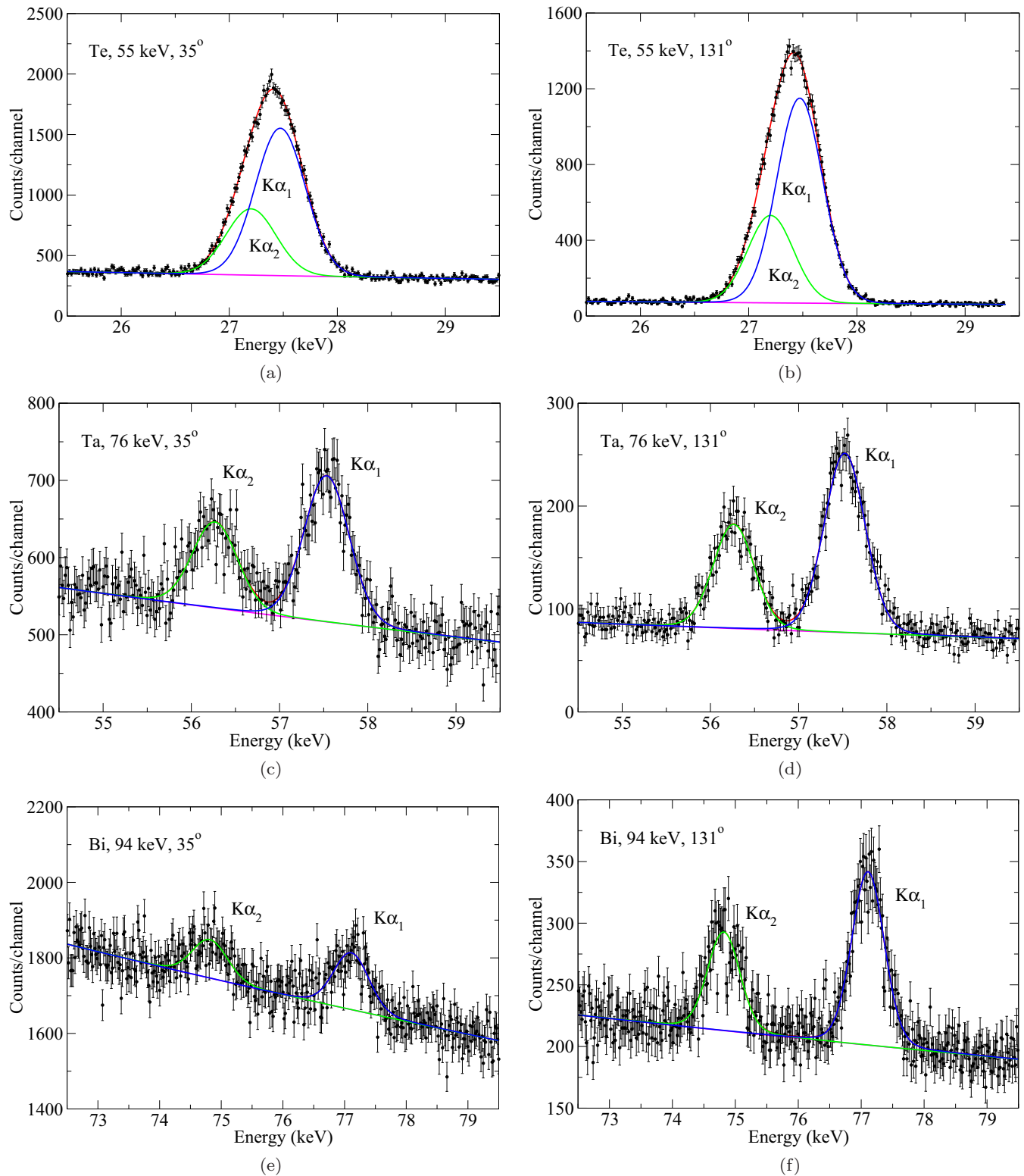


FIG. 2. Regions of the  $K\alpha$  x rays in the energy spectra of Te/C irradiated with (a) and (b) 55-keV electrons, (c) and (d) Ta/C with 76-keV electrons, and (e) and (f) Bi/C with 94-keV electrons. The angle between the detector axis and the beam axis is (a), (c), and (e)  $\theta_1 = 35^\circ$  and (b), (d), and (f)  $\theta_2 = 131^\circ$ . The dots with uncertainty bars (one standard deviation) are the experimental values, whereas the solid curves are the fitted spectra. The energy dispersion is approximately 18 eV/channel in all cases.

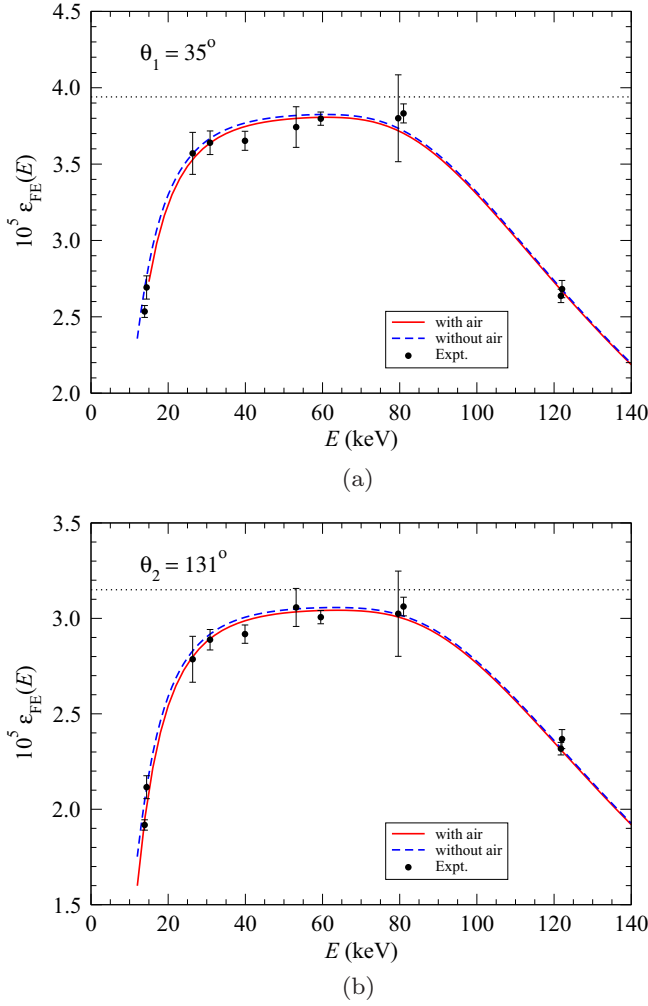


FIG. 3. Full-energy peak efficiencies of the planar HPGe detectors placed at (a)  $\theta_1 = 35^\circ$  and (b)  $\theta_2 = 131^\circ$  with respect to the beam direction. Circles with uncertainty bars (one standard deviation) are experimental values. The curves are the efficiencies calculated with the fitted parameters  $\Omega_i/(4\pi \text{ sr})$  and  $L_i$  ( $i = 1, 2$ ). The solid curves account for attenuator thicknesses (air and Kapton) appropriate to the calibration with radioactive sources, whereas the dashed ones pertain to the electron-beam irradiation conditions (evacuated chamber). The dotted horizontal lines indicate the geometrical efficiencies  $\Omega_i/(4\pi \text{ sr})$  ( $i = 1, 2$ ).

given by [6]

$$\begin{aligned} \sigma_{\text{dir}} &= \frac{16w_0}{p_i^3} \int_0^{E/2} \frac{d\epsilon_e}{p_e p_f} \\ &\times \sum_{\ell_i, \ell_e, \ell_f} \sum_{j_i, j_e, j_f} (2j_i + 1)(2j_e + 1)(2j_f + 1) \\ &\times \mathcal{S}(n_0 \ell_0 j_0, p_i \ell_i j_i \rightarrow p_e \ell_e j_e, p_f \ell_f j_f), \end{aligned} \quad (4)$$

where  $p = \sqrt{2\epsilon + \epsilon^2/c^2}$  and the continuum normalization is  $\sqrt{1 + \epsilon/2c^2}$  times a sine function. Using first-order perturbation theory with only the two-body electrostatic interaction,

the scattering probabilities are [7,25]

$$\begin{aligned} S(0i \rightarrow ef) &= \sum_{\lambda} \frac{F(\lambda)F(\lambda)}{(2j_i + 1)(2j_f + 1)(2j_e + 1)(2j_0 + 1)(2\lambda + 1)} \\ &+ \sum_{\lambda'} \frac{G(\lambda')G(\lambda')}{(2j_i + 1)(2j_f + 1)(2j_e + 1)(2j_0 + 1)(2\lambda' + 1)} \\ &+ 2 \sum_{\lambda, \lambda'} (-1)^{\lambda + \lambda'} \left\{ \begin{matrix} j_f & j_i & \lambda \\ j_e & j_0 & \lambda' \end{matrix} \right\} \\ &\times \frac{F(\lambda)G(\lambda')}{(2j_i + 1)(2j_f + 1)(2j_e + 1)(2j_0 + 1)}, \end{aligned} \quad (5)$$

where the direct multipole function  $F(\lambda)$  and the exchange multipole function  $G(\lambda)$  involve products of two-body electrostatic radial integrals and reduced matrix elements of tensor operators;  $\left\{ \begin{matrix} \cdot & \cdot & \cdot \\ \cdot & \cdot & \cdot \end{matrix} \right\}$  are Wigner  $6j$  symbols. On the other hand, first-order perturbation theory with the full two-body retarded electromagnetic interaction yields the scattering probabilities [7,25]

$$\begin{aligned} S(0i \rightarrow ef) &= \sum_{\lambda, \lambda'} \sum_{\Lambda} \frac{(-1)^{\lambda + \lambda'} F(\lambda, \Lambda) F^*(\lambda', \Lambda)}{(2j_i + 1)(2j_f + 1)(2j_e + 1)(2j_0 + 1)(2\Lambda + 1)} \\ &+ \sum_{\lambda, \lambda'} \sum_{\Lambda} \frac{(-1)^{\lambda + \lambda'} G(\lambda, \Lambda) G^*(\lambda', \Lambda)}{(2j_i + 1)(2j_f + 1)(2j_e + 1)(2j_0 + 1)(2\Lambda + 1)} \\ &+ 2 \sum_{\lambda, \lambda'} \sum_{\Lambda, \Lambda'} (-1)^{\lambda + \lambda'} \left\{ \begin{matrix} j_f & j_i & \Lambda \\ j_e & j_0 & \Lambda' \end{matrix} \right\} \\ &\times \frac{\text{Re}[F(\lambda, \Lambda) G^*(\lambda', \Lambda')]}{(2j_i + 1)(2j_f + 1)(2j_e + 1)(2j_0 + 1)}, \end{aligned} \quad (6)$$

where the direct multipole function  $F(\lambda, \Lambda)$  and the exchange multipole function  $G(\lambda, \Lambda)$  involve products of two-body retarded electromagnetic radial integrals and reduced matrix elements of tensor operators.

The energies and radial wave functions of the bound orbitals were calculated using Grant's Dirac-Fock atomic-structure package [26]. In turn, the continuum radial wave functions were computed by solving the single-channel radial Dirac equation using a distorting potential operator constructed from the atomic-structure bound orbitals.

## V. RESULTS AND DISCUSSION

The experimental  $K$ -shell ionization cross sections for Te, Ta, and Bi and their uncertainties are gathered in Table II. For each energy the tabulated cross section is the average of the values resulting from the measurements done with the two HPGe spectrometers. The measured data and the theoretical SCADW cross sections [25] are shown in Fig. 4.

Regarding the uncertainty budget, Table III lists the contributions of the different factors in Eqs. (1) and (2) to the total uncertainties of the ionization cross sections. We did not include the beam energy among the uncertainty sources because its contribution is negligible. Although in the case of Te the uncertainty of the measured beam energy grows with

TABLE II. *K*-shell ionization cross sections of Te, Ta, and Bi by electron impact (in barns) as a function of energy (in keV). The numbers in parentheses are the uncertainties (one standard deviation) in units of the last significant digits.

Element	<i>E</i> (keV)	$\sigma_K$ (b)
<sup>52</sup> Te	33.56(3)	5.19(26)
<sup>52</sup> Te	35.42(3)	9.4(5)
<sup>52</sup> Te	38.34(3)	15.0(8)
<sup>52</sup> Te	41.26(3)	19.2(9)
<sup>52</sup> Te	45.53(4)	24.3(11)
<sup>52</sup> Te	50.93(4)	28.8(14)
<sup>52</sup> Te	55.28(5)	31.4(16)
<sup>52</sup> Te	60.71(6)	34.5(17)
<sup>52</sup> Te	70.68(6)	37.7(18)
<sup>52</sup> Te	79.93(8)	39.7(19)
<sup>52</sup> Te	90.24(10)	41.1(20)
<sup>52</sup> Te	99.74(14)	41.7(20)
<sup>73</sup> Ta	68.64(3)	0.460(25)
<sup>73</sup> Ta	70.56(3)	1.08(7)
<sup>73</sup> Ta	72.38(3)	1.61(8)
<sup>73</sup> Ta	75.53(3)	2.41(12)
<sup>73</sup> Ta	80.26(3)	3.50(16)
<sup>73</sup> Ta	85.58(3)	4.58(22)
<sup>73</sup> Ta	90.45(3)	5.27(25)
<sup>73</sup> Ta	95.16(3)	5.98(28)
<sup>73</sup> Ta	99.62(3)	6.6(3)
<sup>83</sup> Bi	91.58(3)	0.182(13)
<sup>83</sup> Bi	91.62(3)	0.206(15)
<sup>83</sup> Bi	93.33(3)	0.471(25)
<sup>83</sup> Bi	94.14(3)	0.60(3)
<sup>83</sup> Bi	96.30(3)	0.88(4)
<sup>83</sup> Bi	98.61(3)	1.11(5)
<sup>83</sup> Bi	99.71(3)	1.36(6)

energy (see Table II), above 50 keV the cross section increases smoothly and this uncertainty barely affects that of the cross section. The fast increase of the beam energy standard deviation is a consequence of the procedure implemented for the energy calibration, which used the Te *K* lines as calibration references. On the other hand, the uncertainty associated with  $\omega_K$  was estimated from the fluorescence yields collected in Table 4 of [27] and that of  $\Gamma_{KL_{2,3}}/\Gamma_{K,\text{total}}$  was inferred from the differences between the Dirac-Hartree-Slater [23] and Dirac-Fock [28] ratios of emission rates.

The present measurements for Te and Ta are the first ones close to the respective *K* thresholds. Our experimental values for Bi are consistent with the data reported in [5]. The latter have larger uncertainties because they were obtained with a relative method where the measured ratios of characteristic to bremsstrahlung intensities in the spectra were normalized using theoretical bremsstrahlung differential cross sections whose uncertainties are about 10%. The SCADW ionization cross sections match with the experimental results pertaining to the three studied elements. For the sake of completeness, DWBA [2,3] cross sections are also plotted in Fig. 4. In the case of Te, the DWBA curve is only some 3% lower than the prediction of the SCADW method. However, the difference between the SCADW method and the DWBA increases with

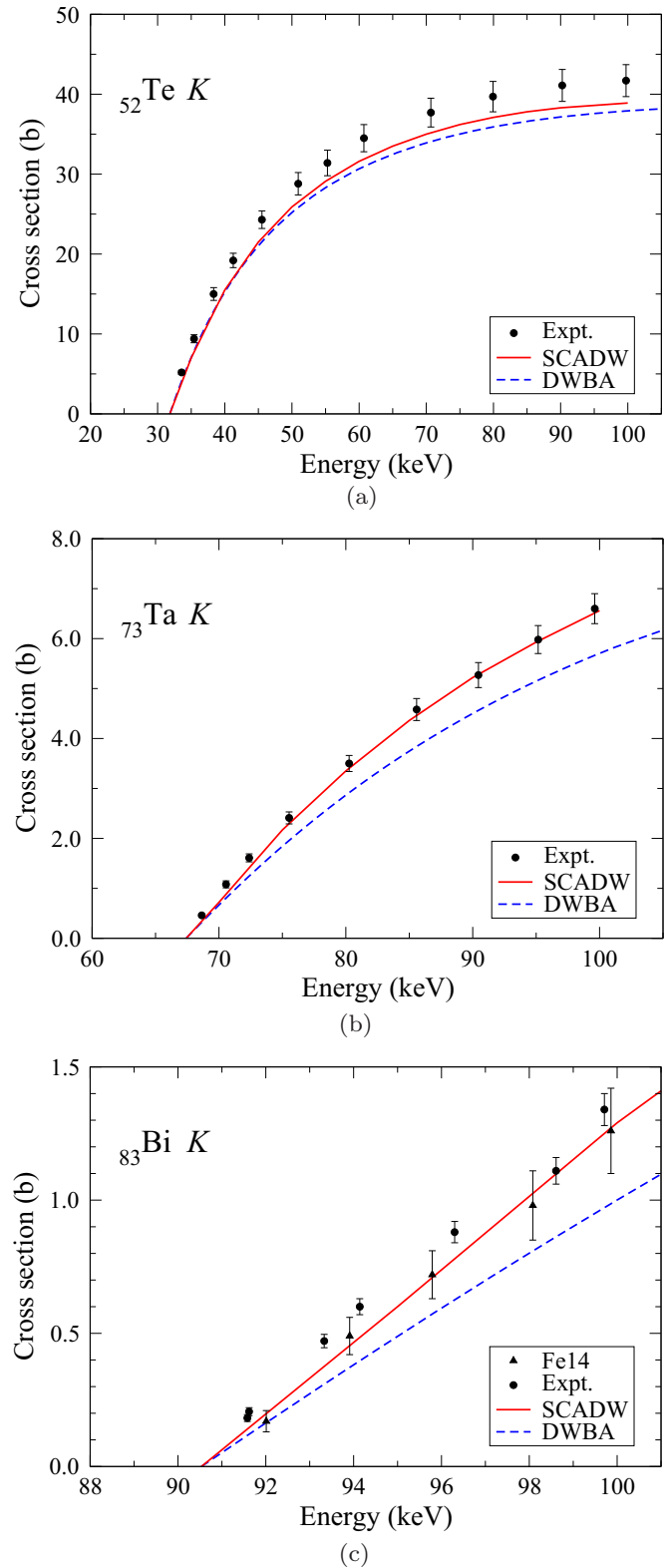


FIG. 4. Ionization cross sections of (a) Te *K*, (b) Ta *K*, and (c) Bi *K* as a function of electron energy. The present experimental values are plotted as circles with uncertainty bars (one standard deviation). The solid and dashed curves are the predictions of the SCADW (full two-body retarded electromagnetic interaction) and DWBA formalisms, respectively. In the case of Bi, the triangles indicate the experimental data from [5].

TABLE III. Contributions of the main uncertainty sources to the standard deviation of the measured cross sections. The factors are identified with the notation used in Eqs. (1) and (2).

Factor	Type <sup>a</sup>	Contribution (%)
$N_{K\alpha}$	A	1–6
$N_e$	A	0.5
$\mathcal{N}d / \cos \alpha$	B <sup>b</sup>	3–4
$\varepsilon_{FE}$	A	1–2
$\tau$	A	<0.5
$\omega_K$	B	1
$\Gamma_{KL_{2,3}} / \Gamma_{K,\text{total}}$	B	2
total		4–8

<sup>a</sup>According to the definitions in [17].

<sup>b</sup>See Table I.

the atomic number of the target atom, reaching around 15% for Ta and 25% for Bi, the SCADW method being consistently closer to experiment than the DWBA.

All experimental cross-section values for Te *K* lie above the SCADW curve by more than one standard deviation. In this case, the predominant source of uncertainty is the areal density (see Tables III and I). Figure 2(a) illustrates that the uncertainty in the counting statistics is small. The measured  $\sigma_K$  values are therefore correlated, which explains why it is possible to draw a smooth curve through the experimental points, whose random fluctuations are much smaller than the uncertainty bars. Note that if we expand the standard deviation of the areal density with a coverage factor  $k = 2$  (95% confidence level), the ensuing uncertainty bars of nearly all measured data intersect the SCADW curve. Hence, we conclude that the experimental Te *K* ionization cross sections are compatible with the SCADW at the  $2\text{-}\sigma$  level.

Llovet *et al.* [1] noted in their review that the experimental data sets of inner-shell ionization cross sections are discrepant for most elements, with variations that may reach (and even exceed) a factor of 2. The difficulties inherent to this type of measurement were discussed at length in [9], and the experimental procedure and the (10–100)-keV beamline of the São Paulo Microtron were designed to overcome most of them [10]. Here we would like to highlight two relevant aspects of the present arrangement. One is the manufacture of very thin targets mounted in C-fiber frames, occupied by the element of interest in the smallest possible area on a thin C backing, thus minimizing both the production and the effect of stray x rays. The other is the determination of the areal density of atoms by RBS, which reduces the uncertainty of this quantity that affects directly the precision of the measured cross sections.

The *ab initio* SCADW and DWBA formalisms are fully relativistic and account for exchange effects. However, while the SCADW method uses distorted waves for the initial, final, and ejected electron states, the DWBA employs plane waves to simplify the evaluation of the transverse interaction. The present measurements clearly show that, for intermediate- to large-*Z* elements the near-threshold *K*-shell ionization cross sections are rather sensitive to the adopted continuum wave functions. This finding is further supported by Fig. 5, where the experimental Au *K* ionization cross sections of two recent

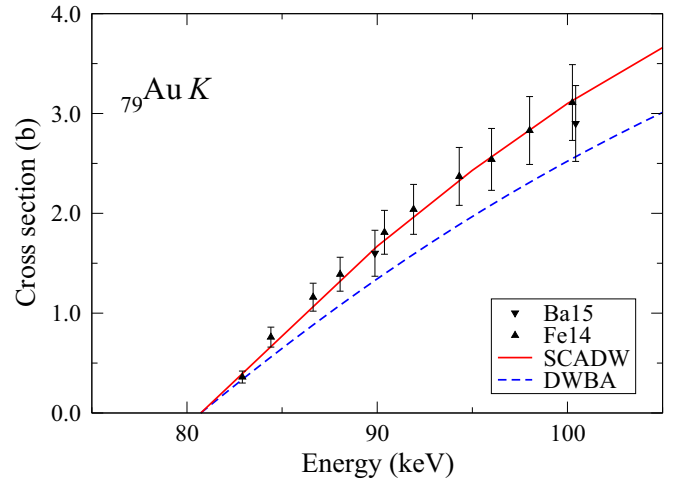


FIG. 5. Ionization cross sections of Au *K* as a function of electron energy. The solid and dashed curves are the predictions of the SCADW (full two-body retarded electromagnetic interaction) and DWBA formalisms, respectively. Up triangles and down triangles indicate the experimental data from [5,29], respectively.

publications [5,29] are compared to the SCADW and DWBA calculations. Again, the SCADW curve agrees with the measured values, while the DWBA is around 15% lower.

To be fair, it should be mentioned that the DWBA performs well near the threshold for the *K* shells of atoms with  $Z \lesssim 50$ . This was confirmed with additional calculations carried out for  $^{47}\text{Ag}$ , where the SCADW and DWBA cross sections agree to within 2% (results not shown). Moreover, ionization cross sections for the Au *L* subshells computed with the SCADW method and DWBA are almost identical [8], and they are compatible with the existing measurements [22,29].

## VI. CONCLUSION

We have measured *K*-shell ionization cross sections for three elements that span a wide range of intermediate and large atomic numbers, namely,  $^{52}\text{Te}$ ,  $^{73}\text{Ta}$ , and  $^{83}\text{Bi}$ . The improved experimental method allowed us to achieve uncertainties below 10%. The SCADW method reproduces satisfactorily these measurements as well as previous Au *K* experimental data. On the other hand, the DWBA cross sections for the *K* shells of atoms with  $Z \gtrsim 50$  appear to be quite sensitive to the choice of projectile-electron wave functions in the evaluation of the transverse interaction. It would be desirable to update the NIST database of electron-impact ionization cross sections with new values calculated using either the SCADW method or an upgraded DWBA code that computed the transverse term with distorted waves for all continuum electron states.

## ACKNOWLEDGMENTS

We thank the staffs of the São Paulo Microtron and the LAMFI accelerators for assistance during the irradiations with the electron and ion beams, respectively. We are indebted to W. G. P. Engel, A. C. Tromba, and S. A. Romero for

helping with the preparation of the targets. This work was performed with funding from the Brazilian agencies Fundação de Amparo à Pesquisa do Estado de São Paulo, through Grant No. 15/14530-7, and Conselho Nacional de Desenvolvimento

Científico e Tecnológico, Grant No. 131658/2014-0. Partial support from the Brazilian Instituto Nacional de Ciência e Tecnologia - Física Nuclear e Aplicações, Project No. 464898/2014-5, is acknowledged.

- 
- [1] X. Llovet, C. J. Powell, F. Salvat, and A. Jablonski, *J. Phys. Chem. Ref. Data* **43**, 013102 (2014).
- [2] D. Bote and F. Salvat, *Phys. Rev. A* **77**, 042701 (2008).
- [3] X. Llovet, F. Salvat, D. Bote, F. Salvat-Pujol, A. Jablonski, and C. J. Powell, *NIST Database of Cross Sections for Inner-Shell Ionization by Electron or Positron Impact* (National Institute of Standards and Technology, Gaithersburg, 2014), Version 1.0.
- [4] F. Salvat, *PENELOPE—2014: A Code System for Monte Carlo Simulation of Electron and Photon Transport* (OECD/NEA, Issy-les-Moulineaux, 2015).
- [5] J. M. Fernández-Varea, V. Jahnke, N. L. Maidana, A. A. Malafrente, and V. R. Vanin, *J. Phys. B* **47**, 155201 (2014).
- [6] M. S. Pindzola and M. J. Buie, *Phys. Rev. A* **37**, 3232 (1988).
- [7] M. S. Pindzola, D. L. Moores, and D. C. Griffin, *Phys. Rev. A* **40**, 4941 (1989).
- [8] M. S. Pindzola, *J. Phys. B* **48**, 015201 (2015).
- [9] V. R. Vanin, M. V. Manso Guevara, N. L. Maidana, M. N. Martins, and J. M. Fernández-Varea, *Radiat. Phys. Chem.* **119**, 14 (2016).
- [10] V. R. Vanin, N. L. Maidana, A. Mangiarotti, R. R. Lima, A. A. Malafrente, S. F. Barros, and M. N. Martins, *Radiat. Phys. Chem.* **154**, 26 (2019).
- [11] T. F. Silva, C. L. Rodrigues, M. Mayer, M. V. Moro, G. F. Trindade, F. R. Aguirre, N. Added, M. A. Rizzutto, and M. H. Tabacniks, *Nucl. Instrum. Methods Phys. Res. Sect. B* **371**, 86 (2016).
- [12] M. Mayer, *Nucl. Instrum. Methods Phys. Res. Sect. B* **332**, 176 (2014).
- [13] R. L. McGreevy and L. Pusztai, *Mol. Sim.* **1**, 359 (1988).
- [14] J. F. Ziegler, M. D. Ziegler, and J. P. Biersack, *Nucl. Instrum. Methods Phys. Res. Sect. B* **268**, 1818 (2010).
- [15] H. H. Andersen, F. Besenbacher, P. Loftager, and W. Möller, *Phys. Rev. A* **21**, 1891 (1980).
- [16] Q. Yang, D. J. O'Connor, and Z. Wang, *Nucl. Instrum. Methods Phys. Res. Sect. B* **61**, 149 (1991).
- [17] BIPM, IEC, IFCC, ISO, IUPAC, IUPAP, and OIML, *Guide to the Expression of Uncertainty in Measurement—Developing and Using Measurement Models* (JCGM, Sèvres, 2008).
- [18] R. D. Deslattes, E. G. Kessler, Jr., P. Indelicato, L. Billy, E. Lindroth, and J. Anton, *Rev. Mod. Phys.* **75**, 35 (2003).
- [19] N. L. Maidana, V. R. Vanin, V. Jahnke, J. M. Fernández-Varea, M. N. Martins, and L. Brualla, *Nucl. Instrum. Methods Phys. Res. Sect. A* **729**, 371 (2013).
- [20] S. M. Seltzer and M. J. Berger, *At. Data Nucl. Data Tables* **35**, 345 (1986).
- [21] L. Kissel, C. A. Quarles, and R. H. Pratt, *At. Data Nucl. Data Tables* **28**, 381 (1983).
- [22] S. F. Barros, V. R. Vanin, N. L. Maidana, M. N. Martins, J. A. García-Alvarez, O. C. B. Santos, C. L. Rodrigues, M. F. Koskinas, and J. M. Fernández-Varea, *J. Phys. B* **51**, 025201 (2018).
- [23] J. H. Scofield, *At. Data Nucl. Data Tables* **14**, 121 (1974).
- [24] M. O. Krause, *J. Phys. Chem. Ref. Data* **8**, 307 (1979).
- [25] M. S. Pindzola, *Phys. Rev. A* **90**, 022708 (2014).
- [26] I. P. Grant, *Relativistic Quantum Theory of Atoms and Molecules* (Springer, Berlin, 2007).
- [27] A. Kahoul, V. Aylikci, N. Kup Aylikci, E. Cengiz, and G. Apaydin, *Radiat. Phys. Chem.* **81**, 713 (2012).
- [28] J. H. Scofield, *Phys. Rev. A* **9**, 1041 (1974).
- [29] S. F. Barros, V. R. Vanin, N. L. Maidana, and J. M. Fernández-Varea, *J. Phys. B* **48**, 175201 (2015).